

Article

# Electro-Catalytic Properties of Palladium and Palladium Alloy Electro-Catalysts Supported on Carbon Nanofibers for Electro-Oxidation of Methanol and Ethanol in Alkaline Medium

Cyril Tlou Selepe <sup>1</sup>, Sandile Surprise Gwebu <sup>1</sup>, Thabo Matthews <sup>1</sup>, Tebogo Abigail Mashola <sup>1</sup>, Ludwe Luther Sikeyi <sup>2</sup>, Memory Zikhali <sup>1</sup>, Siyabonga Patrick Mbokazi <sup>1</sup>, Thobeka Siphon Makhunga <sup>1</sup>, Kayode Adesina Adegoke <sup>1</sup> and Nobanathi Wendy Maxakato <sup>1,\*</sup>

- <sup>1</sup> Department of Chemical Sciences, University of Johannesburg, Doornfontein, Johannesburg 2028, South Africa; cyrilkatlego15@gmail.com (C.T.S.); surprisesgwebu@gmail.com (S.S.G.); matthewsthabo@gmail.com (T.M.); tebogail@gmail.com (T.A.M.); zicaliememo@gmail.com (M.Z.); siyabongambokazi141@gmail.com (S.P.M.); sobahlemut@gmail.com (T.S.M.); kwharyourday@gmail.com (K.A.A.)
- <sup>2</sup> Molecular Sciences Institute, School of Chemistry, University of the Witwatersrand, Braamfontein, Johannesburg 2050, South Africa; ludweluthersikeyi@gmail.com
- \* Correspondence: nmaxakato@uj.ac.za; Tel.: +27-(0)-11-559-6151



**Citation:** Selepe, C.T.; Gwebu, S.S.; Matthews, T.; Mashola, T.A.; Sikeyi, L.L.; Zikhali, M.; Mbokazi, S.P.; Makhunga, T.S.; Adegoke, K.A.; Maxakato, N.W. Electro-Catalytic Properties of Palladium and Palladium Alloy Electro-Catalysts Supported on Carbon Nanofibers for Electro-Oxidation of Methanol and Ethanol in Alkaline Medium. *Catalysts* **2022**, *12*, 608. <https://doi.org/10.3390/catal12060608>

Academic Editor:  
Nicolas Alonso-Vante

Received: 5 April 2022  
Accepted: 16 May 2022  
Published: 2 June 2022

**Publisher's Note:** MDPI stays neutral with regard to jurisdictional claims in published maps and institutional affiliations.



**Copyright:** © 2022 by the authors. Licensee MDPI, Basel, Switzerland. This article is an open access article distributed under the terms and conditions of the Creative Commons Attribution (CC BY) license (<https://creativecommons.org/licenses/by/4.0/>).

**Abstract:** Carbon nanofibers (CNFs) supported by Pd and Pd-Sn electro-catalysts were prepared by the chemical reduction method using ethylene glycol as the reducing agent. Their physicochemical characteristics were studied using high resolution-transmission electron microscopy (HR-TEM), Fourier transform infrared spectroscopy (FTIR), X-ray diffraction (XRD), X-ray photoelectron spectroscopy (XPS), thermogravimetric analysis (TGA) and Bruanaer-Emmett-Teller (BET) analysis. FTIR revealed that oxygen, hydroxyl, carboxylic and carbonyl functional groups facilitated the dispersion of Pd and Sn nanoparticles. The doping of Pd with Sn to generate PdSn alloy was also confirmed by XPS data. The amorphous nature of CNFs was confirmed by XRD patterns which exhibited the Pd diffraction peaks. When Sn was added to Pd/CNFs, the diffraction peaks moved to lower angles. HRTEM images revealed that the CNFs with cylindrical shape-like morphology and also Pd-Sn nanoparticles dispersed on carbon support. The catalytic activity and stability towards alcohol electro-oxidation in alkaline medium at room temperature was evaluated using cyclic voltammetry (CV), chronoamperometry (CA) and electrochemical impedance spectroscopy (EIS). The obtained Pd-Sn/CNFs electro-catalyst exhibited a better electro-catalytic activity than Pd/CNFs and Pd/C electro-catalysts for both methanol and ethanol oxidation. The improvement of the electrochemical performance was associated with the synergistic effect via the addition of Sn which modified the Pd atom arrangement, thereby promoting oxidation through a dehydrogenation pathway. Furthermore, SnO<sub>2</sub> generates abundant OH species which helps with increasing the rate of the oxidative removal of carbon monoxide (CO) intermediates from Pd sites.

**Keywords:** carbon nanofibers; electrocatalyst; methanol; ethanol; cyclic voltammetry; chronoamperometry

## 1. Introduction

Direct alcohol fuel cells (DAFCs) are the most attractive and advanced technology for use as power sources for mobile, stationary and portable applications. DAFCs use liquid fuels which simplify the delivery system, compared to H<sub>2</sub>-fed fuel cells which need a reforming system and have problems with H<sub>2</sub> storage [1,2]. Methanol is recognized as a promising fuel because it can be more easily oxidized than other alcohols. However, sluggish anode kinetics are observed and methanol crossover through the membrane to the cathode side decreases the efficiency [3]. Ethanol is the best alternative fuel because

it is less toxic than methanol and can be produced in larger quantities from biomass. The electro-oxidation of ethanol, on the other hand, is more difficult to achieve than the electro-oxidation of methanol due to difficulties in breaking C-C bonds and the generation of CO intermediates that poison the palladium anode catalyst even in strong alkaline media [4]. The kinetics of an alcohol oxidation reaction can be enhanced by DAFCs in alkaline medium [5]. Furthermore, catalyst materials that are cheaper and more abundant than Pt can be used for alcohol oxidation reactions in alkaline DAFCs [6]. Alkaline anion-exchange membranes (AAEMs) are also used as electrolytes in alkaline DAFCs. Because there are no free hydroxyl ions in the solutions, this electrolyte is believed to protect electrodes from carbonate formation [7].

Therefore, considerable developments in the fabrication of new electro-catalyst materials for the electro-oxidation of methanol and ethanol remain a research hotspot. Pd has proved to be an excellent electro-catalyst for alcohol oxidation in an alkaline media with higher activity and stability than Pt. It is fifty times more prevalent on the planet than Pt [8]. However, owing to the low electro-catalytic activity of Pd in practical DAFCs application, there have been numerous attempts to improve the activity of Pd-based electro-catalysts [9]. Efforts have been made to increase the electro-catalytic performance of Pd in an alkaline media for alcohol oxidation. For example, the addition of oxides such as CeO<sub>2</sub> to Pd/C increase the electro-activity of the electro-catalyst for ethanol oxidation in an alkaline media, compared to the standard E-TEK PtRu/C electro-catalyst [10]. These oxides, such as Ru in PtRu electro-catalysts, are thought to produce OH<sub>ad</sub> species easily. At lower potentials, the OH<sub>ad</sub> species can convert CO-like poisoning species on Pt and Pd to CO<sub>2</sub> or other products that can be dissolved in water, allowing the active sites to be released on Pt and Pd for further electrochemical reactions [11]. Liu et al. [12] employed Pd nanowire arrays to investigate the kinetics of ethanol oxidation in an alkaline medium and discovered that the pH and ethanol concentration had an impact on the oxidation reaction. Because of better Pd utilization, carbon supported gold nanoparticles (Au/C) decorated with a mono- or sub-monolayer of palladium atoms by chemical epitaxial growth approach showed greater specific activity for ethanol oxidation in an alkaline media than Pd/C [13]. Another efficient strategy to mitigate the above problems is to disperse Pd nanoparticles (NPs) onto a suitable support which possesses an extremely high surface area and good electrical conductivity. To control the sizes and morphology of Pd NPs, several carbonaceous materials such as graphene, carbon black, carbon nanotubes (CNTs) and carbon nanofibers (CNFs) have been used. Among them, carbon nanofibers (CNFs), a one-dimensional nanomaterial comprising of sp<sup>2</sup> carbon, are regarded as promising electro-catalyst support [14–16]. The availability and low-cost of CNFs make them one of the most suitable supports for electro-catalysts in DAFCs. Their remarkable properties include an extremely high surface area, good chemical stability, and excellent electronic conductivity [17].

On the other hand, elements such as Sn and Ru have been coupled with Pd to promote electro-activity. Among the mentioned metals, Sn is the least expensive and has previously been combined with Pd to form a binary electro-catalyst, reduce Pd loading and improve electro-catalytic activity [18]. Sn provides oxygen-containing species on the surface that react with the intermediates in the dissociative adsorption of alcohol on the Pd sites. It further modifies the Pd geometric structure, resulting in improved activity [19]. In this paper, we present a straightforward and cost-effective strategy for fabricating a Pd/CNFs electro-catalyst and a co-reduction in metal salts on CNFs to prepare the Pd-Sn/CNFs electro-catalyst. A high porous CNF is used as catalyst support and this carbonaceous material is functionalized prior to modification with the metals. This could be beneficial in improving its electronic structure and chemical reactivity which is expected to control the sizes of metal NPs as well as strengthen the interaction between the metals and carbon support.

## 2. Results and Discussion

### 2.1. Characterisation of Materials

#### 2.1.1. High Resolution-Transmission Electron Microscopy (HRTEM)

HRTEM images of carbon nanofibers, Pd/CNFs and Pd-Sn/CNFs electro-catalysts are presented in Figure 1. The CNF support material exhibits a cylindrical shape-like morphology similar to those of CNTs. However, CNFs have a relatively large diameter and differ in terms of their structural and textural characteristics [20]. CNFs display hollow-core structures with several micrometer-long fibers and an outer diameter of 195.16 nm. As expected, the HRTEM images of Pd/CNFs and Pd-Sn/CNFs electro-catalysts provide evidence that Pd and PdSn nanoparticles are attached to the surface of CNFs (Figure 1B,C). The HRTEM micrographs of the Pd/CNFs electro-catalyst showed some agglomeration of the nanoparticles on the carbon support and the Pd-Sn/CNFs electro-catalyst showed a wide distribution and some agglomeration over the carbon support. The average particle sizes of Pd nanoparticles in Pd/CNFs and Pd-Sn/CNFs electro-catalysts are 7.15 nm and 9.51 nm, respectively. The attachment of Pd and Sn nanoparticles to CNFs occurs through strong interfacial interactions which are not observed in the bulk space of the matrix. The obtained results prove that Pd and Sn nanoparticles are well-connected with the highly conducting CNFs which are requisite for efficient electro-catalyst. The selected area electron diffraction (SAED) patterns of CNFs (D), Pd/CNFs electro-catalyst (E) and Pd-Sn/CNFs electro-catalyst (F) are also shown in Figure 1, thereby supporting the crystallinity of the prepared nanomaterials. It is clear that the nanoparticles corresponding to Pd and Sn are present in these SAED patterns. The (111), (200), (220), and (311) planes of Pd correspond to the Pd face-centered cubic (fcc) structure and are presented by the SAED patterns.

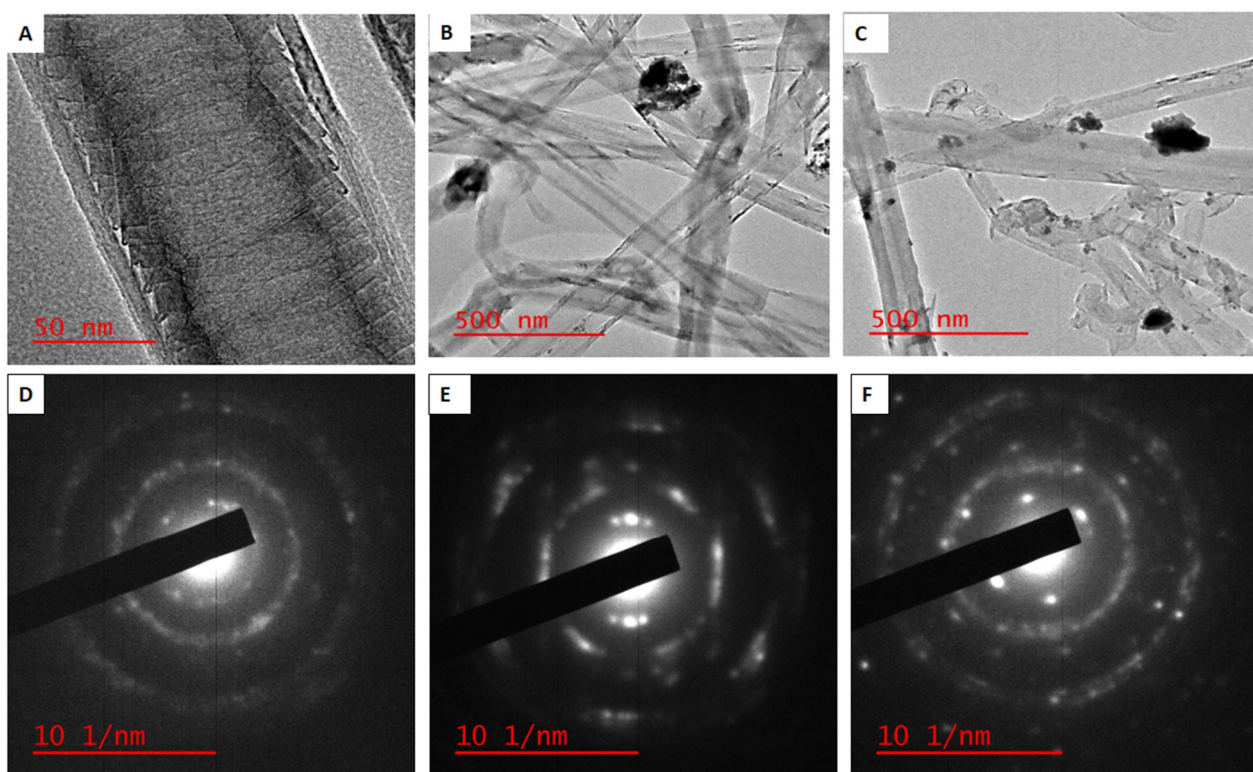


**Figure 1.** HRTEM images of CNFs (A), Pd/CNFs (B) and Pd-Sn/CNFs (C) electro-catalysts; SAED patterns of CNFs (D), Pd/CNFs (E) and Pd-Sn/CNFs (F) electro-catalysts.

#### 2.1.2. Fourier Transform Infrared Spectroscopy (FTIR)

FTIR was used to study the changes of functional groups before and after incorporating Pd and Sn on a CNFs framework. The FTIR spectra of CNFs, Pd/CNFs and Pd-Sn/CNFs

nanomaterials are presented in Figure 2. As expected, the results display the presence of hydroxyl and carboxylic acid groups on the CNFs surface. CNFs exhibit characteristic absorption bands at  $3452\text{ cm}^{-1}$  ascribed to the  $\text{-OH}$  of carboxylic group. The characteristic vibrations at  $2430\text{ cm}^{-1}$  and  $1114\text{ cm}^{-1}$  correspond to the aliphatic  $\text{-CH}$  and  $\text{-CH}_2$  group of CNFs. The band at  $1636\text{ cm}^{-1}$  is assigned to the  $\text{C=O}$  group of the carboxylic acid. The band at  $1386\text{ cm}^{-1}$  is associated with the  $\text{C=C}$  stretching originating from the preparation of the CNFs. The vibration band around  $500\text{ cm}^{-1}$  represents  $\text{Fe-O}$  bond which is due to the residual iron from ferrocene [15,16]. These functional groups are used to facilitate the attachment of Pd and Sn nanoparticles on the CNFs surface. The FTIR spectra of Pd/CNFs and Pd-Sn/CNFs electro-catalysts show identical functional groups to the CNFs spectrum. The disappearance or reduction in bands in CNFs indicate a successful deposition of Pd or Sn on CNF. In addition, the appearance of new bands on Pd-Sn/CNFs show that it is clearly distinctive from that of CNF and Pd/CNF, indicating a successful formation of Pd-Sn alloy on the surface of CNFs and the feasibility of as-obtained electro-catalysts for electro-catalytic application. Sn supplies abundant  $\text{-OH}$  species at interface sites as evidenced by the increase in the intensity of the second peak of  $\text{-OH}$  after the addition of Sn. There is also a vibration between  $650$  and  $500\text{ cm}^{-1}$  due to the  $\text{Sn-O}$  bond.

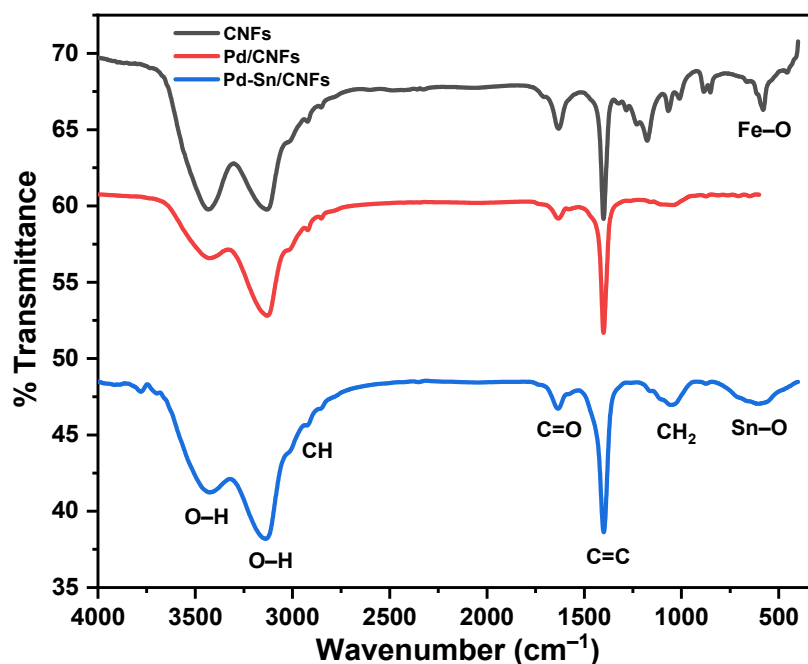


**Figure 2.** FTIR spectra of carbon nanofibers (CNFs) support, Pd/CNFs and Pd-Sn/CNFs electro-catalysts.

### 2.1.3. X-ray Diffraction (XRD)

X-ray diffraction was used to investigate the crystalline structure of CNFs, Pd/CNFs and Pd-Sn/CNFs electro-catalysts shown in Figure 3. The results reveal that the support material is polycrystalline carbon comprised of a defective graphitic crystal lattice. The XRD pattern of CNFs exhibits a typical graphitic, intense and sharp diffraction peak at  $25^\circ$  which represents (002) planes [21]. It is a prominent peak due to the graphitic carbon material. Other graphitic peaks can be seen at  $45^\circ$ ,  $55^\circ$  and  $78^\circ$ , corresponding to the (100 + 101), (004), and (110) planes [22]. It appears that CNF has an ordered structure which is beneficial for improving the electrode electronic conductivity. The XRD pattern of Pd/CNFs shows additional diffraction peaks positioned at the Bragg angles  $40^\circ$ ,  $47^\circ$ ,  $68^\circ$ ,  $84^\circ$  and  $87^\circ$ , corresponding to (111), (200), (220), (311) and (222) lattice planes of Pd. The appearance of these new peaks in the Pd/CNFs nanocomposite demonstrates that Pd nanoparticles were successfully introduced onto the CNFs surface [23]. Furthermore, the XRD pattern of Pd-Sn/CNFs electro-catalyst also displays the diffraction peaks of Pd nanoparticles at the same position. However, these

peaks are broader and less intense, indicating a decrease in particle sizes and an increase in the lattice parameter of palladium. These broad diffraction peaks also confirm the successful introduction of Sn nanoparticles into the CNFs matrix and the formation of PdSn alloy which agrees with the FTIR observation. The average crystalline size of Pd in the Pd-Sn/CNFs electro-catalyst was 1.90 nm, roughly half that of Pd in the Pd/CNFs electro-catalyst (3.91 nm). Due to the alloying of palladium with tin, the lattice parameter of Pd in Pd-Sn/CNFs was 0.8876 nm which is greater than that of Pd in the Pd/CNFs electro-catalyst (0.4716 nm) and the results are presented in Table 1.

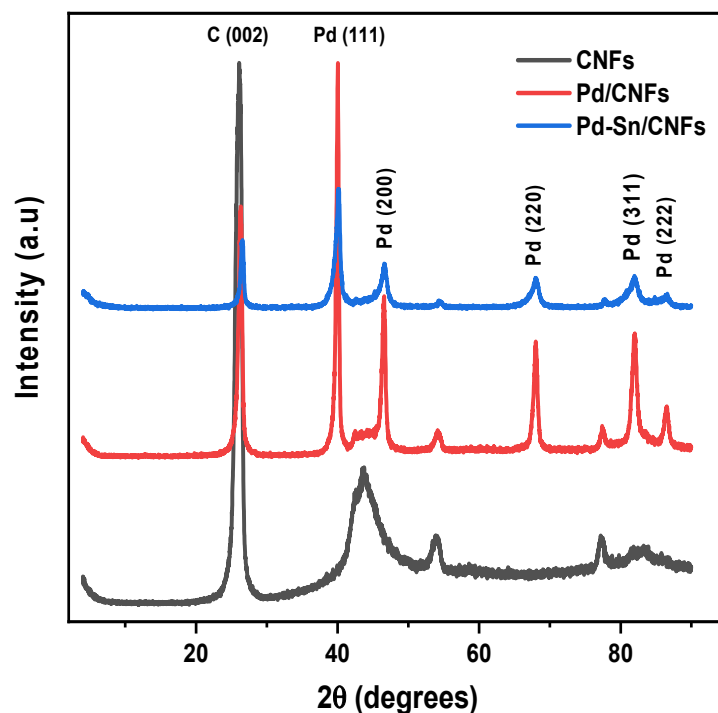


**Figure 3.** XRD patterns of CNFs support, Pd/CNFs and Pd-Sn/CNFs electro-catalysts.

**Table 1.** Average crystal sizes and lattice parameters of Pd in the electro-catalysts.

Electrocatalysts	Pd in Pd/CNFs	Pd in Pd-Sn/CNFs
Average crystal size	3.91 nm	1.90 nm
Lattice parameter	0.4716	0.8876

The average crystalline size of the palladium in the electro-catalysts was calculated from the XRD peak of Pd (111) using the Debye-Scherrer equation:

$$D = \frac{0.9\lambda}{\beta \cos\theta} \quad (1)$$

where  $D$  is the crystalline size, 0.9 is a shape factor,  $\theta$  is the angle of reflection,  $\beta$  is the peak at half maximum and  $\lambda$  is the wavelength of the X-ray [24].

$$\alpha = \frac{(2\sqrt{\lambda})}{\sin\theta} \quad (2)$$

where  $\lambda$  is the wavelength of the X-ray and  $\theta$  is the angle of reflection [24].

### 2.1.4. X-ray Photoelectron Spectroscopy (XPS)

The surface chemistry and electronic structures of the CNF series were investigated using XPS as reported in Figure 4A. The major core levels and the O KVV Auger lines are the only ones that have been labeled. Figure 4B displays the Pd 3d XPS spectra for Pd/CNFs and Pd-Sn/CNFs. The best fit to the experimental data was obtained by adding two spin-orbit doublets (both separated by a spin-orbit splitting of 5.3 eV) and a Shirley type background. These two components can again be ascribed to  $0^+$  and  $2^+$  oxidation states for Pd ions in these compounds [25]. Table 2 shows the fit findings for the binding energy (BE) and spectral weight of the components.

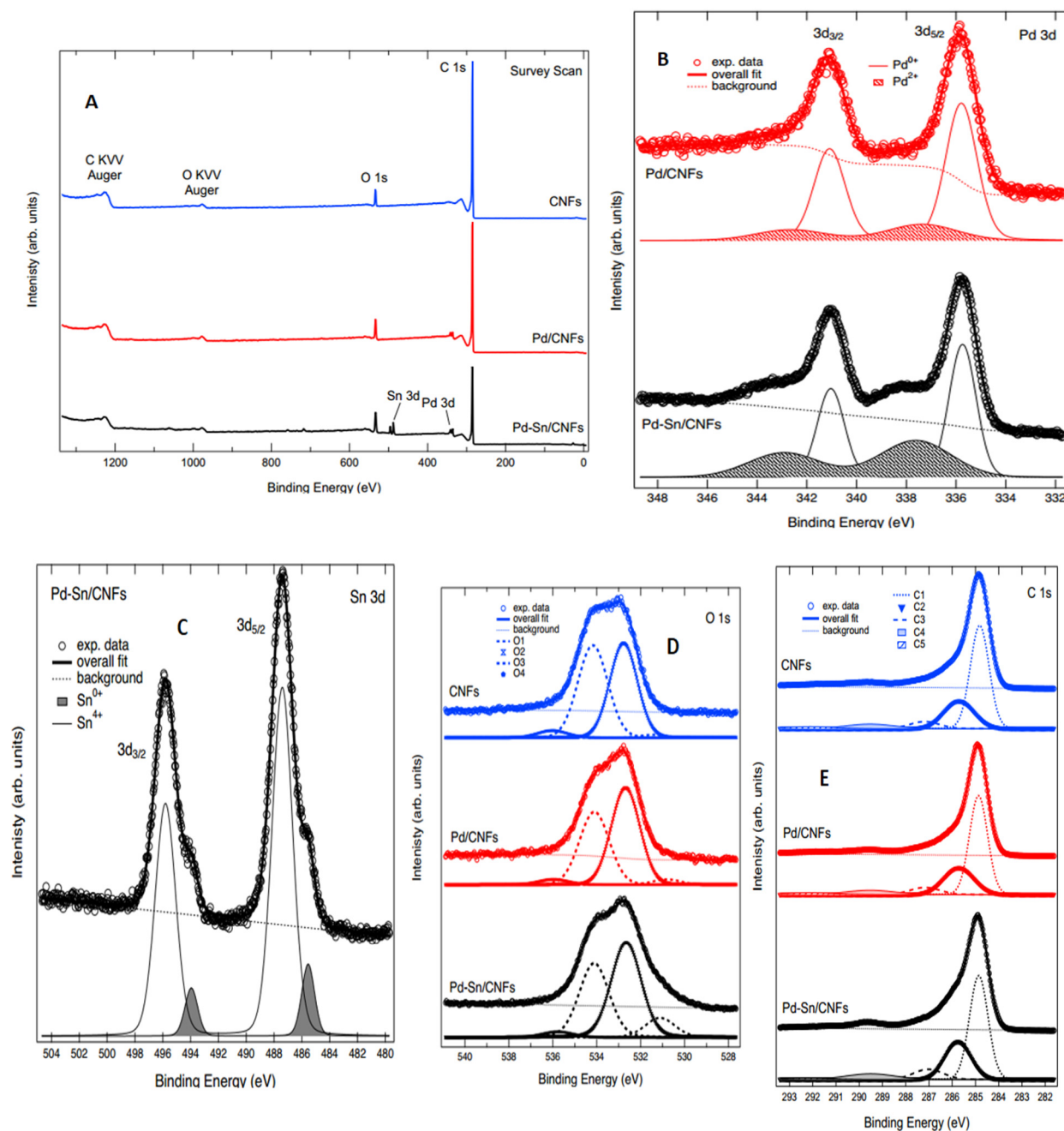


**Figure 4.** XPS spectra (A) survey spectra for (B) Pd 3d for Pd/CNFs and Pd-Sn/CNFs electro-catalysts, (C) Sn 3d for Pd-Sn/CNFs electro-catalyst, (D) O 1s for CNFs, Pd/CNFs and Pd-Sn/CNFs electro-catalysts, (E) C 1s for CNFs, Pd/CNFs and Pd-Sn/CNFs electro-catalysts.

**Table 2.** BEs (eV) and relative percentage areas (%) of the two Pd 3d core level components.

Electrocatalyst	Pd <sup>2+</sup> (eV)	Pd <sup>0+</sup> (eV)	Pd <sup>2+</sup> (%)	Pd <sup>0+</sup>
Pd/CNFs	337.36	335.79	21	79
Pd-Sn/CNFs	337.62	334.74	42	58

The oxidation states of Pd and Sn were also evaluated using XPS. The core level spectrum of Sn 3d for Pd-Sn/CNFs is shown in Figure 4C. The core level has two prominent peaks which correspond to the spin-orbit components of Sn 3d<sub>5/2</sub> and 3d<sub>3/2</sub>. On the low binding energy side of the primary peak, both have a well-defined low-intensity shoulder. As carried out previously, this core level was fitted with two spin-orbit components (separated by a spin-orbit splitting of 8.4 eV) and Shirley background [26]. The binding energy of these components found at 485.55 eV and 487.41 eV for Sn 3d<sub>5/2</sub> are in line with their assignment to 0<sup>+</sup> and 4<sup>+</sup> oxidation states for Sn ions. When the intensities are compared, the 4<sup>+</sup> oxidation state accounts for 87% of the spectral intensity in this core level [27].

Figure 4D shows the core level of O 1s in the CNF samples. As for the CNF samples, adding four Voigt line form singlets provided the best fit to the experimental data to a Shirley background. The attribution of the fitted components for CNF samples are as follows: O1 to C-O bonds, O2 to C=O, O3 to C-O-H/C-O-C bonds and O4 to O-C=O bonds [28]. Table 3 shows the fit findings for binding energy (BE), which indicate excellent alignment amongst the spectra.

**Table 3.** The four components of the O 1s core level's binding energies (eV).

Sample	O1 (eV)	O2 (eV)	O3 (eV)	O4 (eV)
CNFs	531.4	532.79	534.18	536.02
Pd/CNFs	531.3	532.71	534.22	536.07
Pd-Sn/CNFs	531.35	532.75	534.20	536.09

Figure 4E depicts the C 1s core level of the CNF materials. The line shape of the core level is clearly composed of several components. Five Voigt line shape singlets and a Shirley background provided the best fit to the experimental data. The background and the fitted components (labelled C1–C5) are attached to the figure. This line shape was compared to the relevant literature and consistent with the previous set of data, the fitted component can be attributed as follows: C1 to C=C bonds, C2 to C-C bonds, C3 to C-O bonds, C4 to C=O bonds. The extra component C5 can be attributed to carbon ions bonded to F [29]. As presented in Table 4, the fit results for the BE show a good agreement amongst the spectra.

**Table 4.** The five components of the C 1s core level's binding energies (eV).

Sample	C1 (eV)	C2 (eV)	C3 (eV)	C4 (eV)	C5 (eV)
CNFs	284.64	285.78	286.80	289.48	292.13
Pd/CNFs	284.74	285.60	286.90	289.69	292.10
Pd-Sn/CNFs	284.78	285.64	286.88	289.52	292.11

### 2.1.5. Raman Analysis

The Raman spectra of CNF, Pd/CNF and Pd-Sn/CNF electro-catalysts are displayed in Figure 5 and exhibit two prominent bands at 1335 and 1572 cm<sup>-1</sup>. The broad bands correspond to the D and G bands which are attributed to the disorder or defects in the graphite crystal and stretching mode of the C-C bond in the graphite plane [30]. The D-band is due to the disordered carbon. This is caused by C-C vibrations leading to the disruption of the sp<sup>2</sup> hybridized carbon bonds. Graphite is represented by the G-band. The appearance of this peak, which shows the order of graphitic carbons in the structural

matrix of CNFs, is attributed to the in-plane vibration modes of the  $sp^2$  carbon bonds [31]. The obtained spectrum can be attributed to amorphous carbon because the D-band is broad, and the full width at half maximum (FWHM) of the G-band is  $55\text{ cm}^{-1}$ . The calculated intensity ratio of the CNFs support is 0.4, indicating a minimal degree of crystallinity with moderate defects of the carbonaceous material. Concurrently, the ratios of the Pd/CNF and Pd-Sn/CNF electro-catalysts were found to be 0.6 and 0.7, respectively. The electro-catalysts had greater  $I_D/I_G$  values than the CNF supports, indicating that the insertion of Pd and Sn into the CNFs induced defects in the CNF structure and lattice symmetry.

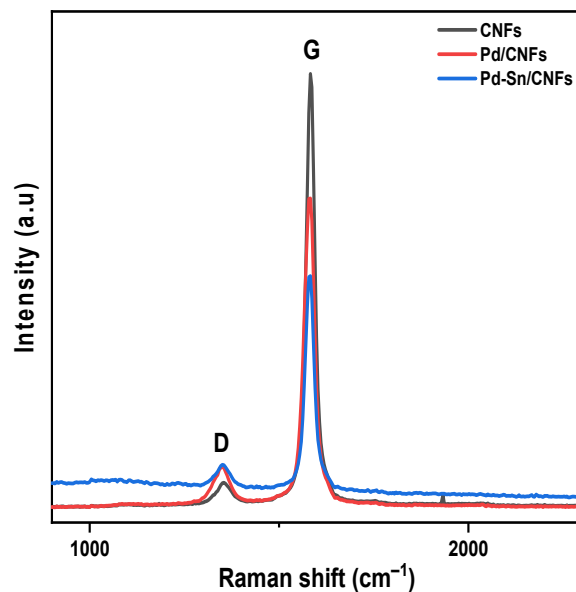


Figure 5. Raman spectrum of carbon nanofibers (CNFs) support, Pd/CNF and Pd-Sn/CNF electro-catalysts.

#### 2.1.6. Thermogravimetric Analysis

A thermogravimetric analysis (TGA) was performed to study the thermal stability of CNFs, Pd/CNFs, and Pd-Sn/CNFs. As illustrated in Figure 6, the TGA profiles of these materials display variable decomposition temperatures. After the decomposition of the CNFs there was no residual mass left, indicating that the material is readily carbon. The initial weight loss observed in the TGA profiles is due to the evaporation of the water molecules due to the adsorption of moisture from the surroundings. CNFs are thermally stable, remaining unchanged across the entire temperature range with no significant mass loss until the initial decomposition around  $560\text{ }^\circ\text{C}$  [28]. Pd/CNFs experienced the first decomposition around  $550\text{ }^\circ\text{C}$ , associated with the species contained within the sample, such as oxygen functional groups. The last two decomposition steps happen at  $570\text{ }^\circ\text{C}$  and  $755\text{ }^\circ\text{C}$ , leading to the decomposition of amorphous carbon and indicating that the nanocomposite has burned out, with a relatively small mass remaining. CNFs are less thermally stable than Pd/CNFs and Pd-Sn/CNFs as indicated by the remaining weight percentages of the electro-catalysts. On the other hand, the Pd-Sn/CNFs had three decomposition temperatures. The first weight loss was around  $540\text{ }^\circ\text{C}$  and was associated with the loss of organic functional groups due to solvent evaporation, including that of water molecules physisorbed onto the compound surface. This indicates the existence of functional groups such as CO, O-C-O, and C-O-C on the surface of CNFs. The second ( $570\text{ }^\circ\text{C}$ ) and final loss ( $780\text{ }^\circ\text{C}$ ) corresponded to the decomposition of amorphous carbon and the loss of the remaining graphitic carbon [25].

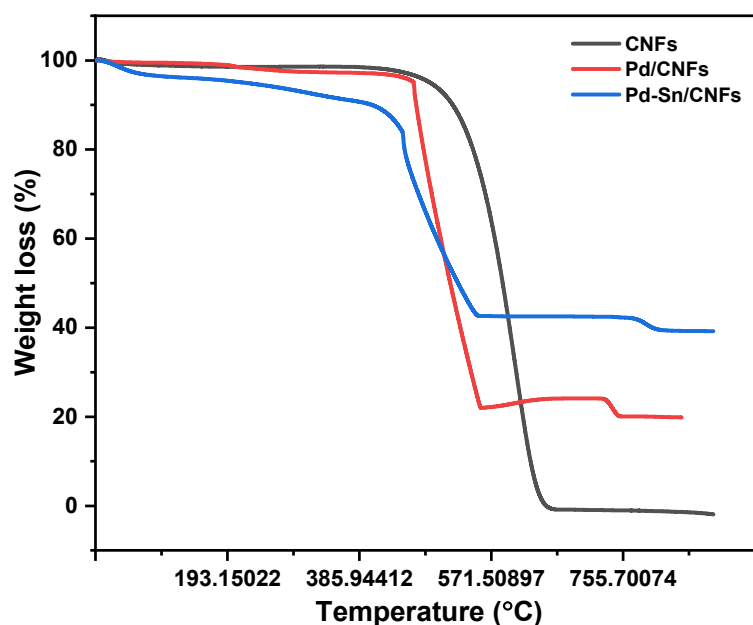


Figure 6. TGA profiles of CNFs support, Pd/CNFs and Pd-Sn/CNFs electro-catalysts.

#### 2.1.7. Brunauer-Emmett-Teller (BET) Surface Area Analysis

BET was used to determine the surface area of the electro-catalyst materials and the results are presented in Table 5. From this table, the surface area decreased as the surface of CNFs was modified with Pd and further decreased after the addition of Sn nanoparticles to the Pd/CNFs catalyst. Barrett, Joyner, and Halenda (BJH) approach was used to analyze the pore-size distribution (PSD) in the desorption branch [32]. PSD revealed that the CNF support exhibits abundant mesopores with a pore diameter of (25.64 nm). The mesoporosity of as-prepared CNFs aided in the achievement of a high metal nanoparticle dispersion. These mesopores for CNF materials help to improve the rate of kinetics and electrolyte ion diffusion [33]. Figure 7 depicts the nitrogen adsorption-desorption isotherms and pore size distribution of CNFs support, and Pd/CNF and Pd-Sn/CNF electro-catalysts. The nitrogen adsorption-desorption isotherms of these nanomaterials were type IV as per IUPAC classification. At  $P/P_0 = 0.7-0.9$ , the H1 hysteresis loops were observed for all the nanomaterials, indicating that the nanomaterials may have a more uniform porous structure. The nature of the hysteresis loop may result from the pore overlap between PdSn and CNFs.

Table 5. BET surface area of CNFs, Pd/CNFs, and Pd-Sn/CNFs.

Nanomaterial	BET Surface Area (m <sup>2</sup> /g)	Pore Volume (cm <sup>3</sup> /g)	Pore Size (nm)
CNFs support	19.6369	1.69	25.64
Pd/CNFs electrocatalyst	18.1912	1.82	27.55
Pd-Sn/CNFs electrocatalyst	17.4183	0.25	42.31

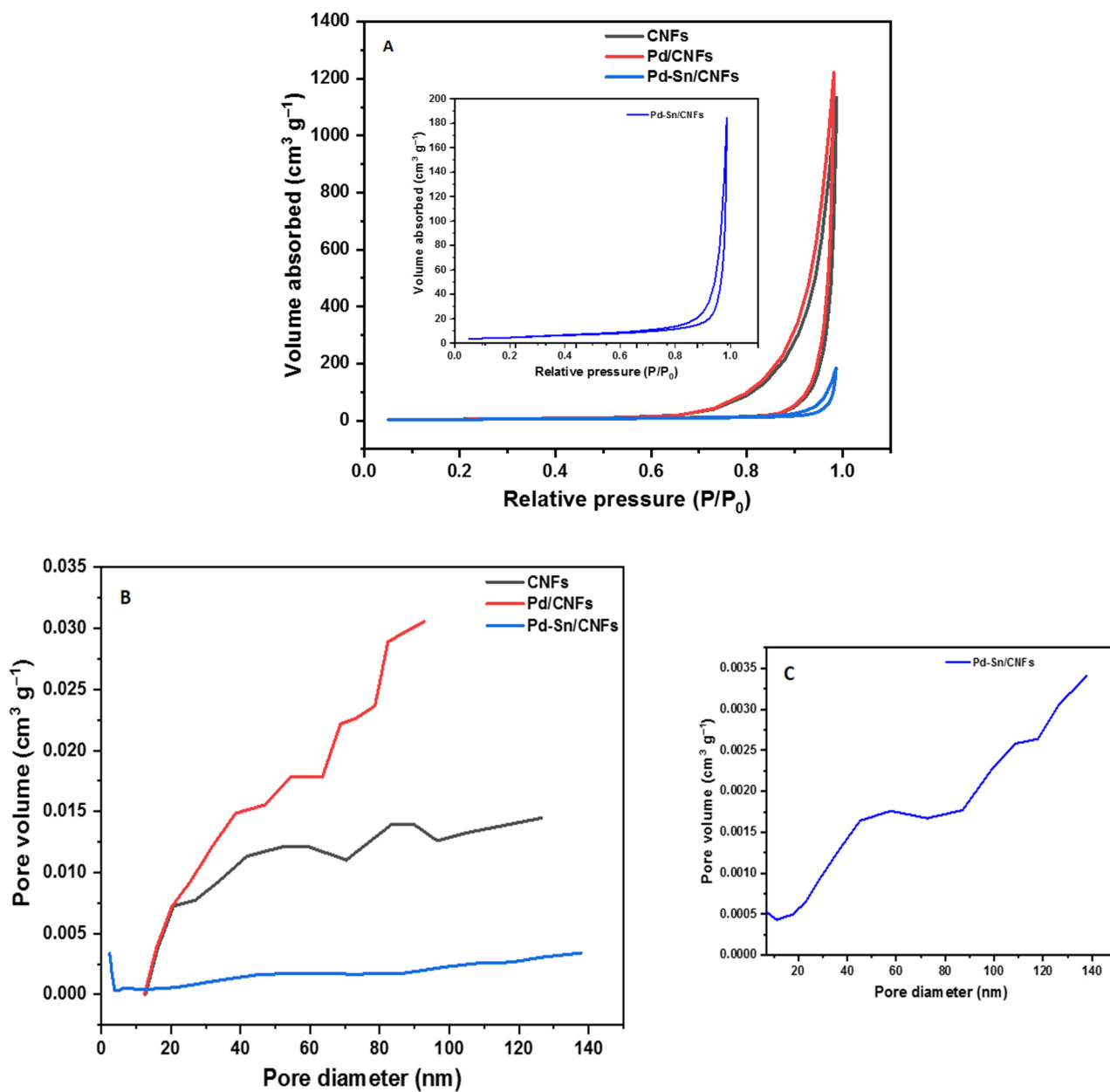


**Figure 7.** Nitrogen adsorption-desorption isotherms of CNFs support, and Pd/CNF and Pd-Sn/CNF (insert) electro-catalysts (A), pore size distributions of CNFs support, and Pd/CNF and Pd-Sn/CNF electro-catalysts (B) and Pd-Sn/CNFs electro-catalyst (C).

## 2.2. Application of Electro-Catalysts in Alcohol Fuel Oxidation Reactions

### 2.2.1. Methanol Electro-Oxidation

#### Cyclic Voltammetric Tests

The CV of the electro-catalysts on the glassy carbon electrode in 1 M KOH is shown in Figure 8a. The OH<sup>-</sup> adsorption peak was observed in all CVs between -0.8 V and 0.4 V while the PdO reduction peak was observed between a 0.4 V and -0.8 V potential window. At -0.5 V, Pd-Sn/CNFs have the highest oxygenated species reduction peak which is useful for methanol oxidation. The electrochemically active surface area (EASA) of the electro-catalysts (Pd/C, Pd/CNFs and Pd-Sn/CNFs) was calculated from the CV curves [34] using the following formula:

$$\text{EASA} = \frac{Q}{sI} \quad (3)$$

where  $Q$  is the Coulombic charge calculated by integrating the area under the PdO reduction peak,  $s$  is the proportionality constant ( $405 \mu\text{C cm}^{-2}$ ) and  $l$  is the Pd loading ( $\text{g cm}^{-2}$ ) [35]. The Pd/C, Pd/CNF and Pd-Sn/CNF electro-catalysts were determined to have EASA values of  $142.94 \text{ cm}^{-2} \text{ mg}^{-1}$ ,  $222.74 \text{ cm}^{-2} \text{ mg}^{-1}$  and  $309.16 \text{ cm}^{-2} \text{ mg}^{-1}$ , respectively. The EASA and electrode surface area were used to normalize CV currents. A large EASA only indicates the presence of more electrochemically active sites on the electro-catalyst surface. Pd-Sn/CNFs and Pd/CNFs electro-catalysts display high values of EASA, compared to that of the Pd/C electro-catalyst. This may be due to the CNFs support and a strong metal-support interaction due to the homogenous dispersion of the PdSn metallic particles over the carbon support.

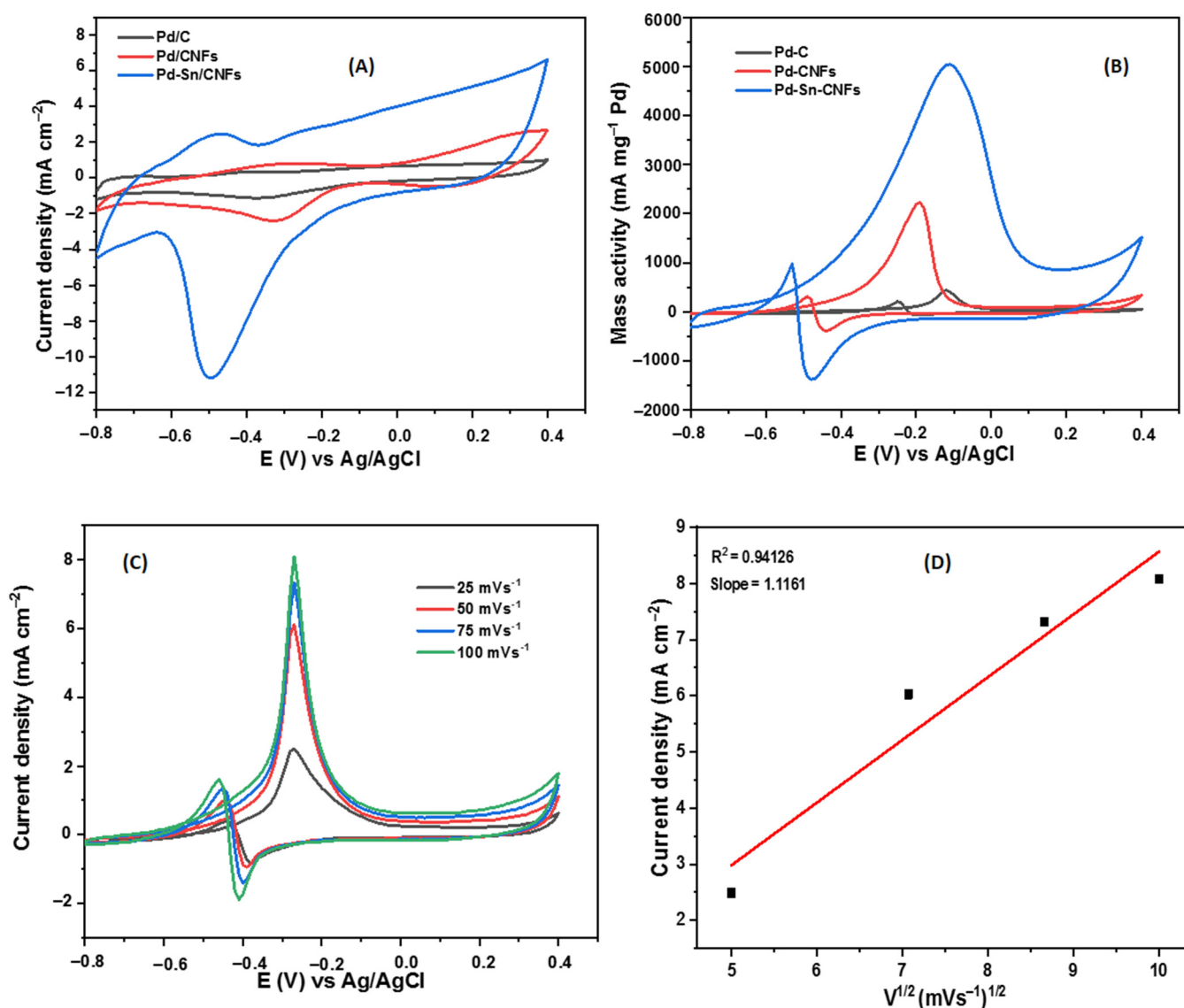


**Figure 8.** (A–D) CV curve of Pd/C, Pd/CNFs and Pd-Sn/CNFs in 1 M KOH (A), in 1 M KOH + 1 M CH<sub>3</sub>OH (B) solution at a scan rate of 50 mVs<sup>-1</sup> at ambient temperature. CV curve of Pd-Sn/CNFs electro-catalyst in 1 M KOH + 1 M CH<sub>3</sub>OH at various scan rates (C) and the relationship between peak current density and scan rates squared (D).

Figure 8B presents the CV curves of Pd/C, Pd/CNF and Pd-Sn/CNF electro-catalysts in the presence of 1 M KOH + 1 M CH<sub>3</sub>OH solution. As illustrated in Figure 8B, Pd/C, Pd/CNF and Pd-Sn/CNF electro-catalysts exhibited two distinct forward and backward current peaks for methanol oxidation reaction. The forward peak is attributed to methanol

oxidation and represents the electro-oxidation of freshly chemisorbed species resulting from adsorbed methanol. The backward peak corresponds to the removal of intermediates incompletely oxidized in the forward scan. The size of the forward peak indicates the electro-catalytic activity for the electro-oxidation reaction of methanol [36]. The results show that the Pd-Sn/CNFs electro-catalyst has a higher electro-catalytic activity for methanol oxidation than Pd/C and Pd/CNF electro-catalysts. The enhanced performance of the Pd-Sn/CNF electro-catalyst may be due to the high surface area and higher Pd dispersion provided by the support material, as well as a faster methanol adsorption and availability of oxygen-containing species (OH) in alkaline medium. The magnitude of the backward peak is less than that of the forward peak in alkaline medium, suggesting that the removal of adsorbed carbonaceous species is easier due to the availability of oxygen-containing species that facilitated the quick methanol oxidation reaction [37,38]. Since Pd-Sn/CNFs outperformed other electro-catalysts prepared in terms of high current, low onset potential and poisoning resistance, further investigation such as the effect of the sweep rate on the current density was investigated.

Figure 8C shows that various scan rate experiments ( $25\text{--}100\text{ mVs}^{-1}$ ) were conducted to assess the electrochemical processes occurring at the glassy carbon electrode surface (either adsorption or diffusion). The obtained result shows that there is a reversible peak because the oxidative and reductive peaks of methanol oxidation are observed. This may be due to the active and sufficient charge transfer rate to maintain the surface equilibrium [39]. The curve of the Pd-Sn/CNFs electro-catalyst shows a behavior of a reversible plot with the stable potential peak as the peak current increases with the increase in scan rates. This stability in potentials may be due to fewer toxic intermediates forming on the electrode surface during methanol oxidation. Despite poisonous species reducing electro-catalyst activity, the Pd-Sn/CNFs electro-catalyst still shows great catalytic activity. This is complemented by the lower oxidation potential and higher current density peak. The processes occurring at the electrode surface were determined by plotting the peak current of each scan rate against the square root of the scan rate shown in Figure 8D. The plot of the Pd-Sn/CNFs electro-catalyst did not have a perfect linear fit graph since electron transfer reactions occur between the electrode and adsorbed molecules on the electrode surface as methanol is oxidized [40].

#### Stability/Durability and Impedimetric Tests

The chronoamperometric technique was used to evaluate the stability and durability of the methanol oxidation reaction on Pd/C, Pd/CNF and Pd-Sn/CNF electro-catalysts. Chronoamperometric measurements were carried out for 2000 s at a fixed potential of 0.5 V in 1 M KOH + 1 M CH<sub>3</sub>OH solution agitated under magnetic stirring at 50 rpm. Figure 9A displays that all the CA curves exhibit a gradual decline in current density, which results from the poisoning of the electro-catalysts by carbon monoxide (CO) intermediate. It is clear that the initial current degradation is rapid for all three electro-catalysts. It is also observed that Pd/CNF and Pd-Sn/CNF electro-catalysts take a much longer time to reach a steady-state, indicating that the electro-catalysts may experience some diffusion layer build-up, thereby leading to depletions of the reactant near the surfaces of the electrodes. In addition, the potentiality of the electro-catalysts to go beyond 2000 s to achieve a perfect plateau is clearly noticeable. The prepared electro-catalysts have a higher current density than that of the commercial Pd/C electro-catalyst. This may be due to CNFs possessing more unique properties than the carbon black, utilization, and content of Pd [41]. The CA curves' y-axis was normalized to convert it to a relative current (%) to better comprehend the electro-catalysts stability and durability. The current loss for the electro-catalysts was 98.9%, 91.5%, and 72.3% for Pd/C, Pd/CNFs, and Pd-Sn/CNFs, respectively, according to the CA curves. The latter had the highest current retention of the electro-catalysts, at 27.5%. Figure S1A shows the methanol oxidation chronoamperometric curves normalized by EASA.

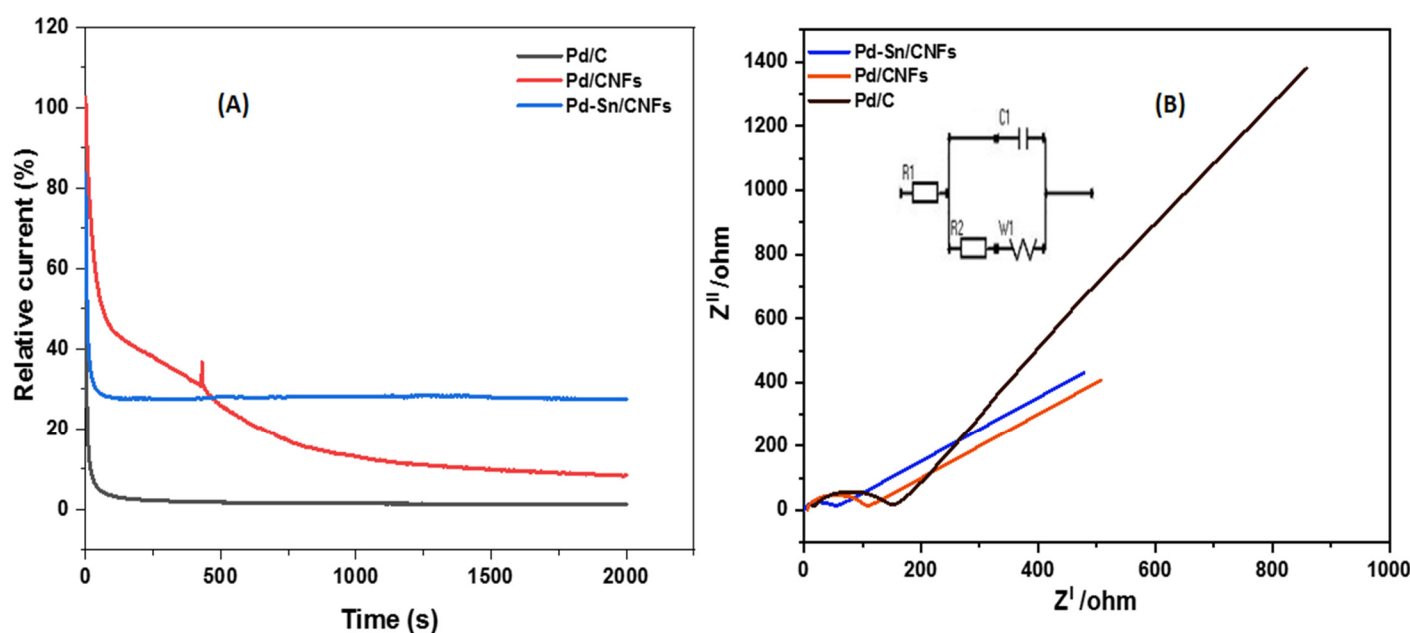


**Figure 9.** Chronoamperometric curves (A) and Nyquist plots of impedance spectra with corresponding equivalent circuit (B) of Pd/C, Pd/CNFs and Pd-Sn/CNFs electro-catalysts at 0.5 V in 1 M KOH + 1 M CH<sub>3</sub>OH solution.

EIS was used to assess the electron transport properties of the modified electrodes for methanol oxidation [42]. The impedance response of Pd/C, Pd-Sn/CNF and Pd/CNF electro-catalysts are illustrated in Figure 9B. Solution resistance (R1), charge transfer resistance (R2), Warburg resistance (W1), and a circuit cell comprise the electrical equivalent circuit. Generally, the presence of a double capacitance layer between the electrolyte and electrode interface is characterized by the presence of the semi-circle at high-frequency regions, whereas the diffusion-limited processes are characterized by the linear segment in the lower frequency region [43]. It is observed that the semi-circles for Pd/C and Pd/CNFs are in the high-frequency region compared to the Pd-Sn/CNFs. This indicates an occurrence of charge transfer reactions on the surface of the electro-catalysts (Pd/CNFs and Pd/C). An increase in charge transfer resistance (Rct) leads to an increase in the semi-circle diameter which results in a slow charge transfer rate (Table 6 shows the resistance values) [44]. The rate of methanol oxidation was faster on the electrode surface in the Pd-Sn/CNFs-modified electrode in comparison with the other electro-catalysts.

**Table 6.** EIS resistance values for electro-catalysts in methanol oxidation.

Electro-Catalyst	R <sub>s</sub> (Ohm)	R <sub>ct</sub> (Ohm)
Pd/C	14.08	67.96
Pd/CNFs	6.28	51.43
Pd-Sn/CNFs	0.43	26.89

## 2.2.2. Ethanol Electro-Oxidation

### Cyclic Voltammetric Tests

Figure 10A displays the CV of Pd/C, Pd/CNF and Pd-Sn/CNF electro-catalysts recorded at a scan rate of 50 mVs<sup>-1</sup> in a solution of 1 M KOH + 1 M CH<sub>3</sub>CH<sub>2</sub>OH. A well-defined oxidation peak can be observed in the three CV curves. The Pd-Sn/CNFs electro-catalyst shows the best catalytic activity and poisoning tolerance among the three catalysts, evidencing by its largest current peak. It is noted that the addition of Sn into Pd/CNFs significantly improves the catalytic activity. This confirms that Sn provides surface oxygen-

containing species that react with intermediates produced during an oxidation reaction. It is apparent that the size effect promotes the higher catalytic activity of Pd-the Sn/CNFs electro-catalyst for ethanol oxidation [45,46]. Since Pd-Sn/CNFs performed better than other electro-catalysts prepared in terms of high current, low onset potential and poisoning tolerance. Based on this, further studies were then carried out on this electro-catalyst by examining the effect of sweep rate on the current density.

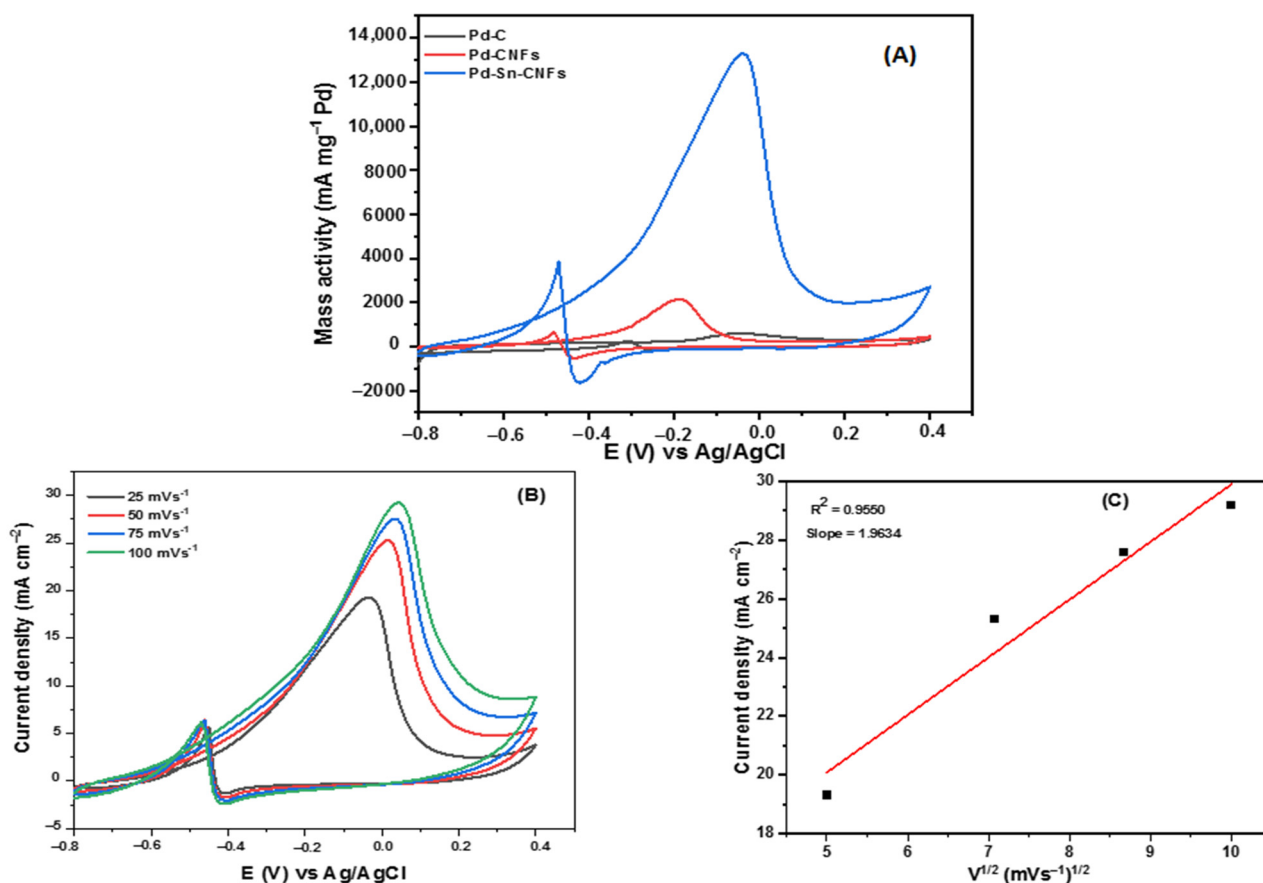


**Figure 10.** CV curve of Pd/C, Pd/CNFs and Pd-Sn/CNFs in 1 M KOH + 1 M CH<sub>3</sub>CH<sub>2</sub>OH (A) solution at a scan rate of 50 mVs<sup>-1</sup> at ambient temperature. CV curve of Pd-Sn/CNFs electro-catalyst in 1 M KOH + 1 M CH<sub>3</sub>CH<sub>2</sub>OH at various scan rates (B) and the relationship between peak current density and scan rates squared (C).

Different scan rate studies (25–100 mVs<sup>-1</sup>) were performed to determine the electrochemical processes at the glassy carbon electrode surface. Figure 10B clearly shows a reversible peak because both oxidation and reduction peaks of ethanol oxidation are observed. This reversibility is due to an active and sufficient charge transfer rate to maintain surface equilibrium [47]. There is a behavior of a reversible plot with peak potential remaining the same in the negative region as the peak current increases with an increase in scan rate. The stability in potential indicates that the Pd-Sn/CNFs electro-catalyst diminishes the build-up of poisonous intermediates formed during ethanol oxidation. The poisonous species has minimal effect on slowing down the activity of the electro-catalyst. This is supplemented by the low onset peak potentials and high peak current density as seen on the CV curves [48]. The plot of the peak current of each scan rate versus the square root of the scan rate was used to determine the processes occurring at the electrode surface. The peak current will be proportional to the square root of the scan rate for a fast electron transfer process with diffusion-reaction taking place [49] as previously explained above.

The straight-line plot of Pd-Sn/CNFs, as seen in Figure 10C, implies that electron transfer reactions occur in a homogenous manner.

### 2.2.3. Stability/Durability and Impedimetric Tests

Figure 11A depicts chronoamperograms of Pd/C, Pd/CNF and Pd-Sn/CNF electro-catalysts in 1 M KOH + 1 M CH<sub>3</sub>CH<sub>2</sub>OH solution at 0.5 V and agitated under magnetic stirring at 50 rpm. The current densities of all electro-catalysts decayed rapidly at the beginning and slowly decayed until a constant state was reached. As the reaction continued, a current steady state was achieved after 400 s. The significant current decrease was caused by the poisoning intermediates adsorbing on the surfaces of the electro-catalysts. The Pd-Sn/CNFs electro-catalyst showed the highest catalytic activity and stability followed by the Pd/CNFs electro-catalyst. Furthermore, the current density of the Pd/CNFs electro-catalyst decayed slower and reached a steady-current after 500 s in comparison with Pd-Sn/CNFs electro-catalyst. The stability of the Pd/C electro-catalyst is inferior compared to other catalysts. The current density decayed rapidly and reached stability near zero [50]. The order of decreasing current loss for the electro-catalysts was 98.6%, 95.4%, and 82.5% for Pd/C, Pd/CNFs, and Pd-Sn/CNFs, respectively, according to the normalized CA curves. In comparison to other materials, the Pd-Sn/CNFs retained 17.8% more current. The oxidation of ethanol chronoamperometric curves normalized by EASA are displayed in Figure S1B.

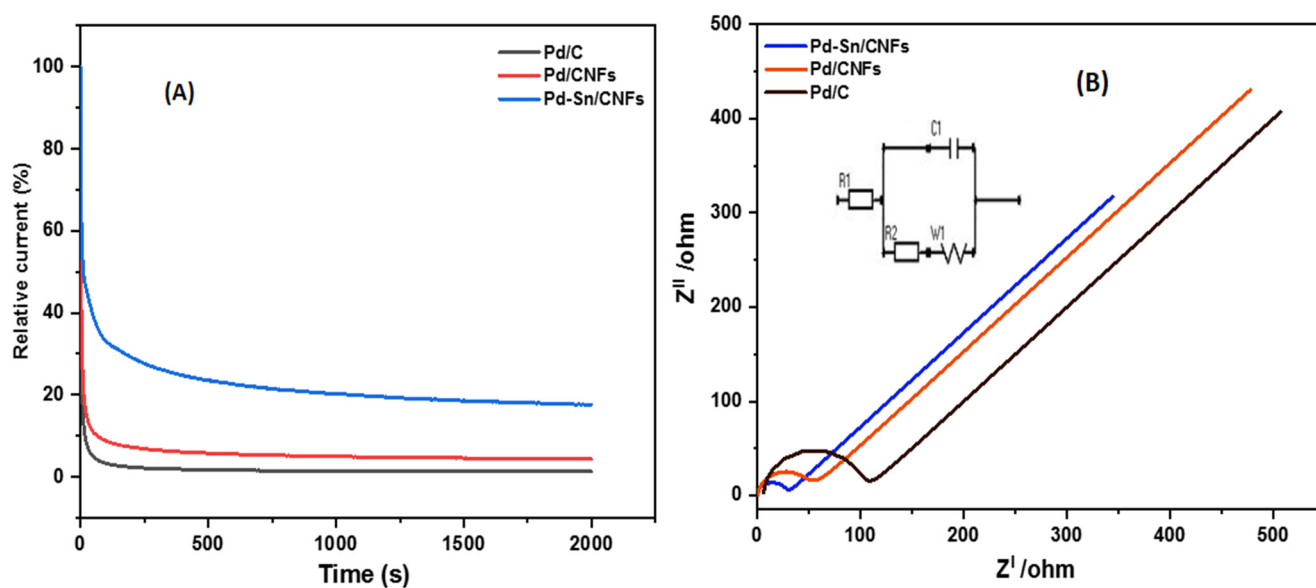


**Figure 11.** Chronoamperometric curves (A) and Nyquist plots of impedance spectra with corresponding equivalent circuit (B) of Pd/C, Pd/CNF and Pd-Sn/CNF electro-catalysts at 0.5 V in 1 M KOH + 1 M CH<sub>3</sub>CH<sub>2</sub>OH solution.

The EIS was used to check the properties of modified electrodes through an in-depth look at the solution interface reactions [51]. As shown in Figure 11B, the catalytic performance of each electro-catalyst for ethanol oxidation reaction was analyzed using EIS. The radius of the impedance arc was used to assess the charge transfer resistance for Pd-Sn/CNF, Pd/CNF and Pd/C electro-catalysts. The semi-circular diameter reflects the charge transfer resistance between the electrolyte and surface of the working electrode when ethanol is oxidized on the GC electrode [52]. The smaller the semi-circular diameter, the smaller the impediment to the electron transfer and the higher the catalytic activity. The Pd-Sn/CNFs electro-catalyst has a smaller semi-circle than other electro-catalysts, indicating the highest catalytic activity (The EIS resistance values are contained in Table 7 below). The EIS results are consistent with the CV results for ethanol oxidation.

**Table 7.** EIS resistance values for electro-catalysts in ethanol oxidation.

Electro-Catalyst	Rs (Ohm)	Rct (Ohm)
Pd/C	6.30	50.06
Pd/CNFs	1.11	27.68
Pd-Sn/CNFs	0.81	14.82

### 3. Materials and Methods

Palladium(II) chloride ( $\text{PdCl}_2$ ) 59–60%; Nafion 117 solution; potassium bromide (KBr) > 99.9%; tin(II) chloride ( $\text{SnCl}_2$ ) 98%; methanol ( $\text{CH}_3\text{OH}$ ) 99.8% were purchased from Sigma Aldrich. Sodium hydroxide pellets (NaOH) 98%; hydrochloric acid (HCl) 37%; Ethanol ( $\text{C}_2\text{H}_5\text{OH}$ ) > 99.9%; sulphuric acid ( $\text{H}_2\text{SO}_4$ ) 95.0–97.0% were supplied by Honeywell and SRL Chemicals. Potassium hydroxide pellets (KOH) 85% and ferrocene ( $\text{C}_{10}\text{H}_{10}\text{Fe}$ ) were obtained from Merck Chemicals. Chicken skins were purchased from Spar supermarket. The reagents were analytical grade and utilized without further modification as received. To make the solutions, we used de-ionized water.

#### 3.1. Synthesis of Carbon Nanofibers (CNFs)

For the growth of CNFs, chicken oil was used as a cheap carbon source and ferrocene ( $\text{C}_{10}\text{H}_{10}\text{Fe}$ ) was used as a catalyst. The chicken oil was obtained by heating chicken skin in an oven at 300 °C to extract oil from its fat. The liquid oil and ferrocene were mixed for 15 min in a small beaker with stirring, then transferred to a silicon substrate (dimensions = 20 × 20 mm, 2 mm thickness) that was placed inside a quartz tube (500 mm long and 45 mm inner diameter) and mounted inside an electric furnace. The suspension was heated for 1 h at a temperature of 600 °C beneath the stream of dilute gas (acetylene and nitrogen). A black deposit (CNFs) formed and was permitted to cool down at ambient temperature and then mechanically crushed to a fine powder [53].

#### 3.2. Functionalization of Carbon Nanofibers (CNFs)

The same functionalization method was reported in our previous study [38].

#### 3.3. Synthesis of Pd/CNFs and Pd-Sn/CNFs Electro-Catalysts

The Pd/CNF and Pd-Sn/CNF electro-catalysts were prepared by the same method described by Selepe CT et al. [38].

#### 3.4. Sample Characterization

HRTEM experiments were performed at an increasing speed voltage of 200 kV using a Jeol JEM-2100F Field Emission Electron Microscope equipped with a LaB6 source. Dropping a small amount of the orchestrated nanocomposite onto a copper grid covered with an elegant carbon film produced the samples. A computerized charge-coupled device (CCD) camera connected to the TEM was used to validate the images of the nanomaterials. FTIR, Model PerkinElmer Spectrum 100 was used to measure the infrared spectra of carbon nanofibers support, Pd/CNF and Pd-Sn/CNF electro-catalysts in the frequency range of 500–4000  $\text{cm}^{-1}$ . Raman spectra were acquired with a T64000 series II triple spectrometer system from HORIBA scientific, Jobin Yvon Technology. XRD measurements of CNF, Pd/CNF and Pd-Sn/CNF nanomaterials. Cu  $\text{K}\alpha$  radiation ( $\lambda = 0.15405$  nm) was used to make measurements in the  $2\theta$  range from 5 to 90° at 40 kV and 40 mA operational conditions. For surface area analysis, BET, Micromeritics TriStar II Plus, Germany was utilized. Thermogravimetric analysis was conducted using (TGA, Hitachi-STA7200RV, Japan) for thermal stability determination. The chosen heat rate was 20 °C/min with a temperature range between 25 and 800 °C under a nitrogen environment. XPS (model Kratos Axis Ultra DLD) was utilized to distinguish the elemental composition and electronic

state of palladium and tin within the carbon nanofibers using an Al (monochromatic) anode, furnished with charge neutralizer.

### 3.5. Electrochemical Characterisation

#### 3.5.1. Electrode Preparation

A total of 10 mg of electro-catalysts was dissolved in 2 mL ethanol with 5  $\mu$ L of Nafion solution. The dried pre-treated glassy carbon electrode (GCE) was drop-coated with 15  $\mu$ L of the ink prepared by sonicating the above-mentioned solution for 15 min. The latter was polished on Micro cloth TM (Buehler, Lake Bluff, IL, USA) with 1.0, 0.3, and 0.05  $\mu$ m alumina slurries in order before drop-coating. To eliminate loose particles from the micro cloth, it was sonicated with double distilled water. Electrochemical characterizations were assessed utilizing an Ivium Technologies Com-pactstat.h standard and a three-electrode system. The potentials of the working electrode were established using the reference (Ag/AgCl) and counter (Pt wire) electrodes saturated with 3 M NaCl. The results were compared to a Pd/C standard electro-catalyst of 10 wt.% which was tested under the same conditions.

#### 3.5.2. Electrochemical Measurements

The Ivium Technologies Com-pactstat.h standard and 3-electrode system were used to conduct electrochemical experiments. The working electrode's potentials were obtained using a 3 M NaCl-saturated reference (Ag/AgCl) and counter (Pt wire) electrodes. The improved GCE's working surface area was 0.07 cm<sup>-2</sup> during the electrochemical experiments. Fifteen minutes before the electrochemical tests, the alkaline electrolyte solution was purged with argon. The chronoamperometric experiments were conducted as the solution was agitated under magnetic stirring at 50 rpm. This was performed in order to maintain the solution near the electrode homogeneous. The results were compared to a Pd/C electro-catalyst with a content of 10 wt.% that was tested under the same conditions.

## 4. Conclusions

Pd/CNF and Pd-Sn/CNF electro-catalysts were prepared using the alcohol reduction method. This proved to be an effective method to fabricate an active electro-catalyst for methanol and ethanol oxidation in an alkaline medium. The Pd-Sn/CNFs exhibited superior electro-catalytic activity and stability compared to other electro-catalysts in both methanol and ethanol electro-oxidation. The electro-catalytic behaviors of the present study were also compared with the conventional Pd/C electro-catalyst. The oxidation of methanol on Pd-Sn/CNFs does not have a perfect linear fit graph due to electron transfer reactions occurring between the electrode and adsorbed molecules on the electrode surface. Meanwhile, ethanol on Pd-Sn/CNFs occurred quickly, as validated by the proportional relationship of the peak current with the square root of the scan rate of Pd-Sn/CNFs with a slope close to 0.5, indicating the presence of a diffusion-controlled reaction. EIS further supplemented a fast kinetics reaction which showed that the reactions on Pd-Sn/CNFs are faster than other electro-catalysts. The high catalytic activity of Pd-Sn/CNFs for the electro-oxidation of both alcohols is attributed to the uniform dispersion of Pd nanoparticles on the CNFs surface and good alloying with Sn nanoparticles. As a result, the electro-catalysts that were developed offer a lot of potential for electrochemical energy conversion and storage applications.

**Supplementary Materials:** The following are available online at <https://www.mdpi.com/article/10.3390/catal12060608/s1>, Figure S1. Chronoamperograms (A) of Pd/C, Pd/CNF and Pd-Sn/CNF electro-catalysts at 0.5 V in 1 M KOH + 1 M CH<sub>3</sub>OH solution and (B) of Pd/C, Pd/CNF and Pd-Sn/CNF electro-catalysts at 0.5 V in 1 M KOH + 1 M CH<sub>3</sub>CH<sub>2</sub>OH solution.

**Author Contributions:** Conceptualization, C.T.S. and N.W.M.; methodology, C.T.S. and L.L.S.; software, T.M.; validation, C.T.S., S.S.G. and T.M.; formal analysis, N.W.M. and K.A.A.; investigation, T.A.M.; resources, N.W.M.; data curation, T.M.; writing—original draft preparation, C.T.S.; writing—review and editing, C.T.S., M.Z. and S.P.M.; visualization, S.S.G., T.M. and T.S.M.; supervision, N.W.M.; project administration, C.T.S.; funding acquisition, N.W.M. All authors have read and agreed to the published version of the manuscript.

**Funding:** This research was funded by National Research Foundation of South Africa (grant number NRF-TTK 118148), University Research Council, Department of Science and Technology and National Nanoscience Postgraduate Teaching and Training Programme (NNPTTP).

**Data Availability Statement:** Data are available on request. Please contact Nobanathi W. Maxakato, +27-83-513-4598, nmaxakato@uj.ac.za.

**Acknowledgments:** During the research and writing of the publication, the authors warmly recognize the efforts and support offered by the Electrochemistry group, Centre for Nanomaterials Science Research, Department of Chemical Sciences, University of Johannesburg, South Africa. The authors are grateful to the funding parties that have supported this research financially since its inception.

**Conflicts of Interest:** The authors declare no conflict of interest.

## References

1. Sikeyi, L.L.; Matthews, T.; Adekunle, A.S.; Maxakato, N.W. Electro-oxidation of Ethanol and Methanol on Pd/C, Pd/CNFs and Pd–Ru/CNFs Nanocatalysts in Alkaline Direct Alcohol Fuel Cell. *Electroanalysis* **2020**, *32*, 2681–2692. [[CrossRef](#)]
2. Zakaria, Z.; Kamarudin, S.; Timmiati, S. Membranes for direct ethanol fuel cells: An overview. *Appl. Energy* **2016**, *163*, 334–342. [[CrossRef](#)]
3. Wang, B.; Tao, L.; Cheng, Y.; Yang, F.; Jin, Y.; Zhou, C.; Yu, H.; Yang, Y. Electrocatalytic oxidation of small molecule alcohols over Pt, Pd, and Au catalysts: The effect of alcohol's hydrogen bond donation ability and molecular structure properties. *Catalysts* **2019**, *9*, 387. [[CrossRef](#)]
4. Gwebu, S.; Nomngongo, P.; Mashazi, P.; Nyokong, T.; Maxakato, N. Platinum nanoparticles supported on carbon nanodots as anode catalysts for direct alcohol fuel cells. *Int. J. Electrochem. Sci.* **2017**, *12*, 6365–6378. [[CrossRef](#)]
5. An, L.; Zhao, T.; Shen, S.; Wu, Q.; Chen, R. Performance of a direct ethylene glycol fuel cell with an anion-exchange membrane. *Int. J. Hydrogen Energy* **2010**, *35*, 4329–4335. [[CrossRef](#)]
6. Yu, E.H.; Wang, X.; Krewer, U.; Li, L.; Scott, K. Direct oxidation alkaline fuel cells: From materials to systems. *Energy Environ. Sci.* **2012**, *5*, 5668–5680. [[CrossRef](#)]
7. Kim, J.; Momma, T.; Osaka, T. Cell performance of Pd–Sn catalyst in passive direct methanol alkaline fuel cell using anion exchange membrane. *J. Power Sources* **2009**, *189*, 999–1002. [[CrossRef](#)]
8. Jiang, L.; Hsu, A.; Chu, D.; Chen, R. Ethanol electro-oxidation on Pt/C and PtSn/C catalysts in alkaline and acid solutions. *Int. J. Hydrogen Energy* **2010**, *35*, 365–372. [[CrossRef](#)]
9. Huang, H.; Wang, X. Recent progress on carbon-based support materials for electrocatalysts of direct methanol fuel cells. *J. Mater. Chem. A* **2014**, *2*, 6266–6291. [[CrossRef](#)]
10. Hu, F.; Chen, C.; Wang, Z.; Wei, G.; Shen, P.K. Mechanistic study of ethanol oxidation on Pd–NiO/C electrocatalyst. *Electrochim. Acta* **2006**, *52*, 1087–1091. [[CrossRef](#)]
11. Shen, S.; Zhao, T.; Xu, J.; Li, Y. Synthesis of PdNi catalysts for the oxidation of ethanol in alkaline direct ethanol fuel cells. *J. Power Sources* **2010**, *195*, 1001–1006. [[CrossRef](#)]
12. Liu, J.; Ye, J.; Xu, C.; Tong, Y. Kinetics of ethanol electrooxidation at Pd electrodeposited on Ti. *Electrochem. Commun.* **2007**, *9*, 2334–2339. [[CrossRef](#)]
13. Zhu, L.; Zhao, T.; Xu, J.; Liang, Z. Preparation and characterization of carbon-supported sub-monolayer palladium decorated gold nanoparticles for the electro-oxidation of ethanol in alkaline media. *J. Power Sources* **2009**, *187*, 80–84. [[CrossRef](#)]
14. Qin, Y.-H.; Jia, Y.B.; Jiang, Y.; Niu, D.F.; Zhang, X.S.; Zhou, X.G.; Niu, L.; Yuan, W.K. Controllable synthesis of carbon nanofiber supported Pd catalyst for formic acid electrooxidation. *Int. J. Hydrogen Energy* **2012**, *37*, 7373–7377. [[CrossRef](#)]
15. Faghihian, H.; Kooravand, M.; Atarodi, H. Synthesis of a novel carbon nanofiber structure for removal of lead. *Korean J. Chem. Eng.* **2013**, *30*, 357–363. [[CrossRef](#)]
16. Maddah, B.; Soltaninezhad, M.; Adib, K.; Hasanzadeh, M. Activated carbon nanofiber produced from electrospun PAN nanofiber as a solid phase extraction sorbent for the preconcentration of organophosphorus pesticides. *Sep. Sci. Technol.* **2017**, *52*, 700–711. [[CrossRef](#)]
17. Bhardwaj, N.; Kundu, S.C. Electrospinning: A fascinating fiber fabrication technique. *Biotechnol. Adv.* **2010**, *28*, 325–347. [[CrossRef](#)]
18. Li, S.; Dong, Z.; Yang, H.; Guo, S.; Gou, G.; Ren, R.; Zhu, Z.; Jin, J.; Ma, J. Microenvironment Effects in Electrocatalysis: Ionic-Liquid-Like Coating on Carbon Nanotubes Enhances the Pd-Electrocatalytic Alcohol Oxidation. *Chem.—Eur. J.* **2013**, *19*, 2384–2391. [[CrossRef](#)]

19. Du, W.; Mackenzie, K.E.; Milano, D.F.; Deskins, N.A.; Su, D.; Teng, X. Palladium–tin alloyed catalysts for the ethanol oxidation reaction in an alkaline medium. *ACS Catal.* **2012**, *2*, 287–297. [[CrossRef](#)]
20. Suriani, A.B.; Dalila, A.R.; Mohamed, A.; Isa, I.M.; Kamari, A.; Hashim, N.; Soga, T.; Tanemura, M. Synthesis of carbon nanofibres from waste chicken fat for field electron emission applications. *Mater. Res. Bull.* **2015**, *70*, 524–529. [[CrossRef](#)]
21. Ramos, A.; Cameán, I.; García, A.B. Graphitization thermal treatment of carbon nanofibers. *Carbon* **2013**, *59*, 2–32. [[CrossRef](#)]
22. Cameán, I.; García, A.B.; Suelves, I.; Pinilla, J.L.; Lázaro, M.J.; Moliner, R. Graphitized carbon nanofibers for use as anodes in lithium-ion batteries: Importance of textural and structural properties. *J. Power Sources* **2012**, *198*, 303–307. [[CrossRef](#)]
23. Souza, F.M.; Parreira, L.; Hammer, P.; Batista, B.; Santos, M. Niobium: A promising Pd co-electrocatalyst for ethanol electrooxidation reactions. *J. Solid State Electrochem.* **2018**, *22*, 1495–1506. [[CrossRef](#)]
24. Vigier, F.; Coutanceau, C.; Hahn, F.; Belgsir, E.; Lamy, C. On the mechanism of ethanol electro-oxidation on Pt and PtSn catalysts: Electrochemical and in situ IR reflectance spectroscopy studies. *J. Electroanal. Chem.* **2004**, *563*, 81–89. [[CrossRef](#)]
25. Wang, J.; Liu, L.; Chou, S.; Liu, H.; Wang, J. A 3D porous nitrogen-doped carbon-nanofiber-supported palladium composite as an efficient catalytic cathode for lithium–oxygen batteries. *J. Mater. Chem. A* **2017**, *5*, 1462–1471. [[CrossRef](#)]
26. Li, G.; Pickup, P.G. Decoration of carbon-supported Pt catalysts with Sn to promote electro-oxidation of ethanol. *J. Power Sources* **2007**, *173*, 121–129. [[CrossRef](#)]
27. Li, H.; Sun, G.; Cao, L.; Jiang, L.; Xin, Q. Comparison of different promotion effect of PtRu/C and PtSn/C electrocatalysts for ethanol electro-oxidation. *Electrochim. Acta* **2007**, *52*, 6622–6629. [[CrossRef](#)]
28. Hu, G.; Nitze, F.; Sharifi, T.; Barzegar, H.R.; Wågberg, T. Self-assembled palladium nanocrystals on helical carbon nanofibers as enhanced electrocatalysts for electro-oxidation of small molecules. *J. Mater. Chem.* **2012**, *22*, 8541–8548. [[CrossRef](#)]
29. Nitze, F.; Abou-Hamad, E.; Wågberg, T. Carbon nanotubes and helical carbon nanofibers grown by chemical vapour deposition on C60 fullerene supported Pd nanoparticles. *Carbon* **2011**, *49*, 1101–1107. [[CrossRef](#)]
30. Wang, L.; Ju, J.; Deng, N.; Wang, G.; Cheng, B.; Kang, W. ZnS nanoparticles anchored on porous carbon nanofibers as anode materials for lithium ion batteries. *Electrochem. Commun.* **2018**, *96*, 1–5. [[CrossRef](#)]
31. Zou, G.; Zhang, D.; Dong, C.; Li, H.; Xiong, K.; Fei, L.; Qian, Y. Carbon nanofibers: Synthesis, characterization, and electrochemical properties. *Carbon* **2006**, *44*, 828–832. [[CrossRef](#)]
32. Villarroel-Rocha, J.; Barrera, D.; Sapag, K. Introducing a self-consistent test and the corresponding modification in the Barrett, Joyner and Halenda method for pore-size determination. *Microporous Mesoporous Mater.* **2014**, *200*, 68–78. [[CrossRef](#)]
33. Jeong, J.H.; Lee, Y.H.; Kim, B.-H. Relationship between microstructure and electrochemical properties of 2lignin-derived carbon nanofibers prepared by thermal treatment. *Synth. Met.* **2020**, *260*, 116287. [[CrossRef](#)]
34. Oldham, K.B. Ultimate cyclic voltammetry: An analytical examination of the reversible case. *J. Solid State Electrochem.* **2013**, *17*, 2749–2756. [[CrossRef](#)]
35. Fischer, D.A.; Vargas, I.T.; Pizarro, G.E.; Armijo, F.; Walczak, M. The effect of scan rate on the precision of determining corrosion current by Tafel extrapolation: A numerical study on the example of pure Cu in chloride containing medium. *Electrochim. Acta* **2019**, *313*, 457–467. [[CrossRef](#)]
36. Zhao, J.; Zhang, L.; Xue, H.; Wang, Z.; Hu, H. Methanol electrocatalytic oxidation on highly dispersed platinum–ruthenium/graphene catalysts prepared in supercritical carbon dioxide–methanol solution. *RSC Adv.* **2012**, *2*, 9651–9659. [[CrossRef](#)]
37. Bachiller-Baeza, B.; Peña-Bahamonde, J.; Castillejos-López, E.; Guerrero-Ruiz, A.; Rodríguez-Ramos, I. Improved performance of carbon nanofiber-supported palladium particles in the selective 1,3-butadiene hydrogenation: Influence of carbon nanostructure, support functionalization treatment and metal precursor. *Catal. Today* **2015**, *249*, 63–71. [[CrossRef](#)]
38. Selepe, C.T.; Gwebu, S.S.; Matthews, T.; Mashola, T.A.; Sikeyi, L.L.; Zikhali, M.; Maxakato, N.W. Effect of Sn Doping on Pd Electro-Catalysts for Enhanced Electro-Catalytic Activity towards Methanol and Ethanol Electro-Oxidation in Direct Alcohol Fuel Cells. *Nanomaterials* **2021**, *11*, 2725. [[CrossRef](#)]
39. Raseruthe, K.E.; Matthews, T.; Gwebu, S.S.; Pillay, K.; Maxakato, N.W. Investigating the effect of carbon support on palladium-based catalyst towards electro-oxidation of ethylene glycol. *Mater. Res. Express* **2021**, *8*, 015017. [[CrossRef](#)]
40. Karuppasamy, L.; Lee, G.-J.; Anandan, S.; Wu, J.J. Synthesis of shape-controlled Pd nanocrystals on carbon nanospheres and electrocatalytic oxidation performance for ethanol and ethylene glycol. *Appl. Surf. Sci.* **2020**, *519*, 146266. [[CrossRef](#)]
41. Yan, Z.; He, G.; Shen, P.K.; Luo, Z.; Xie, J.; Chen, M. MoC–graphite composite as a Pt electrocatalyst support for highly active methanol oxidation and oxygen reduction reaction. *J. Mater. Chem. A* **2014**, *2*, 4014–4022. [[CrossRef](#)]
42. Wang, Y.; Wang, L.; Chen, H.; Hu, X.; Ma, S. Fabrication of highly sensitive and stable hydroxylamine electrochemical sensor based on gold nanoparticles and metal–metalloporphyrin framework modified electrode. *ACS Appl. Mater. Interfaces* **2016**, *8*, 18173–18181. [[CrossRef](#)] [[PubMed](#)]
43. Jiao, J.; Zuo, J.; Pang, H.; Tan, L.; Chen, T.; Ma, H. A dopamine electrochemical sensor based on Pd–Pt alloy nanoparticles decorated polyoxometalate and multiwalled carbon nanotubes. *J. Electroanal. Chem.* **2018**, *827*, 103–111. [[CrossRef](#)]
44. Soundararajan, D.; Park, J.; Kim, K.; Ko, J. Pt–Ni alloy nanoparticles supported on CNF as catalyst for direct ethanol fuel cells. *Curr. Appl. Phys.* **2012**, *12*, 854–859. [[CrossRef](#)]
45. Sharma, S. Recent developments in electrocatalysts and hybrid electrocatalyst support systems for polymer electrolyte fuel cells. In *Electrocatalysts for Low Temperature Fuel Cells: Fundamentals and Recent Trends*; Wiley-VCH: Weinheim, Germany, 2017; pp. 197–239.

46. Cao, L.; Sun, G.; Li, H.; Xin, Q. Carbon-supported IrSn catalysts for direct ethanol fuel cell. *Fuel Cells Bull.* **2007**, *2007*, 12–16. [[CrossRef](#)]
47. Ning, L.; Liu, X.; Deng, M.; Huang, Z.; Zhu, A.; Zhang, Q.; Liu, Q. Palladium-based nanocatalysts anchored on CNT with high activity and durability for ethanol electro-oxidation. *Electrochim. Acta* **2019**, *297*, 206–214. [[CrossRef](#)]
48. Hosseini, M.G.; Mahmoodi, R.; Daneshvari-Esfahlan, V. Ni@Pd core-shell nanostructure supported on multi-walled carbon nanotubes as efficient anode nanocatalysts for direct methanol fuel cells with membrane electrode assembly prepared by catalyst coated membrane method. *Energy* **2018**, *161*, 1074–1084. [[CrossRef](#)]
49. Zhang, J.; She, Y. Mechanism of methanol decomposition on the Pd/WC (0001) surface unveiled by first-principles calculations. *Front. Chem. Sci. Eng.* **2020**, *14*, 1052–1064. [[CrossRef](#)]
50. Fayomi, O.; Daniyan, A.; Umoru, L.; Popoola, A. Data on the effect of current density relationship on the super-alloy composite coating by electrolytic route. *Data Brief* **2018**, *18*, 776–780. [[CrossRef](#)]
51. Choudhury, A.; Chandra, H.; Arora, A. Application of solid oxide fuel cell technology for power generation—A review. *Renew. Sustain. Energy Rev.* **2013**, *20*, 430–442. [[CrossRef](#)]
52. Pan, Y.; Wang, T.-Y.; Yan, X.-M.; Xu, X.W.; Zhang, Q.D.; Zhao, B.L.; El Hamouti, I.; Hao, C.; He, G.-H. Benzimidazolium functionalized polysulfone-based anion exchange membranes with improved alkaline stability. *Chin. J. Polym. Sci.* **2018**, *36*, 129–138. [[CrossRef](#)]
53. Sikeyi, L.; Adekunle, A.; Maxakato, N. Electro-catalytic activity of carbon nanofibers supported palladium nanoparticles for direct alcohol fuel cells in alkaline medium. *Electrocatalysis* **2019**, *10*, 420–428. [[CrossRef](#)]